Spectral element method for band structures of two-dimensional anisotropic photonic crystals

Ma Luo,[1,2] Qing Huo Liu,[1] and Zhibing Li[2]
[1]*Department of Electrical and Computer Engineering, Duke University, Durham, North Carolina 27708, USA*
[2]*The State Key Laboratory of Optoelectronic Materials and Technologies, School of Physics and Engineering, Sun Yat-Sen University, Guangzhou, 510275, People's Republic of China*

(Received 21 November 2008; revised manuscript received 11 January 2009; published 12 February 2009)

A spectral element method (SEM) is proposed for the accurate calculation of band structures of two-dimensional anisotropic photonic crystals. It uses Gauss-Lobatto-Legendre polynomials as the basis functions in the finite-element framework with curvilinear quadrilateral elements. Coordination mapping is introduced to make the curved quadrilateral elements conformal with the problem geometry. Mixed order basis functions are used in the vector SEM for full vector calculation. The numerical convergence speed of the method is investigated with both square and triangular lattices, and with isotropic and in-plane anisotropic media. It is shown that this method has spectral accuracy, i.e., the numerical error decreases exponentially with the order of basis functions. With only four points per wavelength, the SEM can achieve a numerical error smaller than 0.1%. The full vector calculation method can suppress all spurious modes with nonzero eigenvalues, thus making it easy to filter out real modes. It is thus demonstrated that the SEM is an efficient alternative method for accurate determination of band structures of two-dimensional photonic crystals.

DOI: 10.1103/PhysRevE.79.026705 PACS number(s): 02.70.Hm, 42.70.Qs, 42.25.Fx, 52.40.Db

I. INTRODUCTION

Photonic crystals (PCs) are a kind of artificial material made of a periodic array of dielectric materials [1–3]. Compared to a uniform dielectric material, PCs have different energy spectra versus wave vector, which is known as band structures of PCs. For some particular PCs, photonic band gaps (PBGs) exist within the band structures. An optical wave with frequency inside the PBGs cannot propagate through the periodic material within these band gaps. This property makes such a PC a perfect mirror for optical waves within the frequency band gaps. Such properties of PCs have motivated many researchers to investigate various methods to produce waveguides and resonant cavities of extremely high-Q factors using PCs [4].

Accurate determination of the band structures of photonic crystals is a critical step in the design of PCs. One can either solve Maxwell's equations or the Helmholtz equation to obtain the electromagnetic fields in a PC system. Three commonly used methods for the determination of band structures of photonic crystals are the finite-difference frequency-domain (FDFD) [5], finite element method (FEM) [13,14], and the plane-wave expansion (PWE) [6,7] methods to solve Maxwell's equations or the equivalent Helmholtz equation. In the FDFD method, the Yee grid is used to spatially discretize the system with a structured mesh. The PWE method discretizes the system in the reciprocal wave vector space. The FEM uses an unstructured mesh to discretize the space. These methods have been found to yield good results for the determination of the band structures, but they usually require a large number of points per wavelength (PPW) in order to obtain accurate results. For example, in our experience, the FDFD and FEM require at least 10 PPW to have numerical error smaller than 1%; such relatively slow numerical convergence is due to the use of relatively low-order (first-order) basis functions (or equivalent basis functions in the FDFD method), or because of field discontinuities at the material interfaces (PWE). These traditional methods have second-order accuracy or less.

Recently, the pseudospectral time-domain (PSTD) and pseudospectral frequency-domain (PSFD) methods [8–11] have been introduced to computational electromagnetics to calculate electromagnetic fields with high accuracy. The determination of band structure of PCs was solved by [12] using a multidomain pseudospectral method solver (PSMS). It was demonstrated that the PSMS can achieve much higher accuracy than the conventional methods such as PWE and FDFD. The multidomain PSMS can deal with spatially abrupt changes of permittivity without losing the accuracy.

In this paper, we propose an alternative method for accurate determination of band structures based on the spectral element method (SEM) with high convergence speed. The basic principle of SEM is similar to FEM, but with different choice of basis functions and quadrature integration. In our scheme of SEM, all elements are quadrilateral in 2D, and the basis functions are constructed by Gauss-Lobatto-Legendre (GLL) polynomials [15–17]. The quadrilateral elements can be either straight or curved depending on the problem geometry. The basis functions in real space are mapped to the basis functions in the reference domain by curvilinear mapping. By increasing the order of the GLL polynomials for the basis functions, the accuracy increases exponentially, while the number of basis functions increases slowly. Therefore, the SEM can have higher accuracy and fewer basis functions compared to the FEM. It is well known that when the scalar FEM is used to solve a full vector field equation, the method is flawed with the present of spurious modes with non-zero eigenvalues. We apply a mixed order scheme for the choice of basis functions for SEM, which can suppress all the spurious modes having nonzero eigenvalues, which is similar to the edge-element-based FEM.

We apply this SEM to two-dimensional (2D) arrays of dielectric rods or air columns in 2D PCs by solving the Helmholtz equation for the z component of electric (magnetic) field in the TM (TE) mode. The medium can be inho-

mogeneous and anisotropic on the xy plane (i.e., in-plane anisotropy). We show that with only four points per wavelength, the SEM can achieve a numerical error smaller than 0.1%. We also apply the full vector mixed order SEM to calculate eigenmodes of 2D PCs with nonzero z components of wave vectors.

The paper is organized as follow. In Sec. II, the Helmholtz equation is introduced for anisotropic media, and the detail of SEM is explained, including its GLL basis functions, discretization, curvilinear mapping, and mixed order SEM for full vector calculation. In Sec. III, numerical results of square lattice and triangular lattice PCs are shown, together with an anisotropic PC controlled by an applied magnetic field, and a square lattice PC with a z-component wave vector. Section IV gives a brief conclusion.

II. FORMULATION

A. The 2D Helmholtz equations and SEM functionals for anisotropic PCs

For a 2D electromagnetic problem in a medium with in-plane anisotropy, the solution can be separated to two kinds of modes: the TM mode and TE mode. For the TM mode, only E_z, H_x, and H_y are nonzero, so that a scalar Helmholtz equation for the electric field E_z can be formulated from Maxwell's equations

$$\nabla \times [\mu_{rs}^{-1}(\nabla \times E_z\hat{z})] - k_0^2\varepsilon_{rz}E_z\hat{z} = 0, \tag{1}$$

where $k_0=\omega/c$ is wave number in vacuum, $\nabla=\hat{x}\frac{\partial}{\partial x}+\hat{y}\frac{\partial}{\partial y}$, $\mu_{rs}=\left[\begin{smallmatrix}\mu_{xx} & \mu_{xy}\\ \mu_{yx} & \mu_{yy}\end{smallmatrix}\right]$ is the relative in-plane anisotropic permeability, and ε_{rz} is the relative permittivity in the z direction. For PCs, the solution of this wave equation is a Bloch wave. As a result, the electric field can be expressed as

$$E_z = U_E(x,y)e^{i\mathbf{k}\cdot\mathbf{r}}, \tag{2}$$

where $U_E(x,y)$ is a periodic function according to the corresponding lattice structure, and $\mathbf{k}$ is the Bloch wave vector. In order to apply the SEM, we should formulate the functional for a variational method. This can be achieved by the integration of the dot product of field $E_z^*\hat{z}$ (an asterisk denotes complex conjugation) and the left-hand side of Eq. (1). After integration by parts and making use of the periodic boundary condition, the functional can be written as

$$F(E_z) = \int_\Gamma d\mathbf{r}\{(\nabla \times E_z^*\hat{z}) \cdot [\mu_{rs}^{-1}(\nabla \times E_z\hat{z})] - k_0^2\varepsilon_{rz}E_z^*E_z\}, \tag{3}$$

where Γ is the domain of integration, in this case the unit cell of a PC. Note that the boundary surface integral term vanishes because of the Bloch boundary condition at the unit cell surface.

Similarly, for the TE mode, the scaler Helmholtz equation of magnetic field H_z is

$$\nabla \times [\varepsilon_{rs}^{-1}(\nabla \times H_z\hat{z})] - k_0^2\mu_{rz}H_z\hat{z} = 0, \tag{4}$$

where $\varepsilon_{rs}=\left[\begin{smallmatrix}\varepsilon_{xx} & \varepsilon_{xy}\\ \varepsilon_{yx} & \varepsilon_{yy}\end{smallmatrix}\right]$ is the relative in-plane anisotropic permittivity and μ_{rz} is the relative permeability in the z direction. The solution can be expressed as a Bloch wave as

$$H_z = U_H(x,y)e^{i\mathbf{k}\cdot\mathbf{r}} \tag{5}$$

and the functional is

$$F(H_z) = \int_\Gamma d\mathbf{r}\{(\nabla \times H_z^*\hat{z}) \cdot [\varepsilon_{rs}^{-1}(\nabla \times H_z\hat{z})] - k_0^2\mu_{rz}H_z^*H_z\}. \tag{6}$$

These functionals will be used in the SEM to arrive at discrete equations.

When the material is arbitrary anisotropic instead of in-plane anisotropic, or when the wave number along $\hat{z}$ direction is not zero, the TM mode and TE mode will couple to each other. In this case, the full vector version of Helmholtz equation of electric field is needed to describe the problem

$$\nabla \times [\mu^{-1}(\nabla \times \mathbf{E})] - k_0^2\varepsilon\mathbf{E} = 0, \tag{7}$$

where μ and ε are both 3×3 matrices. In order to keep the continuity of tangential components of electric field, we write the field in the form of $\mathbf{E}=\mathbf{U}(x,y)e^{ik_zz}$ instead of $\mathbf{U}_0(x,y)e^{i\mathbf{k}_\parallel\cdot\mathbf{r}}e^{ik_zz}$, where $\mathbf{U}(x,y)$ is a periodic vector function with Bloch periodical boundary condition. In the case of a square lattice PC, the cell is square, and then the boundary condition is given as

$$\mathbf{U}_\parallel(x+a,y) = \mathbf{U}_\parallel(x,y)e^{ik_xa},$$

$$\mathbf{U}_\parallel(x,y+a) = \mathbf{U}_\parallel(x,y)e^{ik_ya}, \tag{8}$$

where $\mathbf{U}_\parallel$ is the tangential component of $\mathbf{U}$. In the case of triangular lattice PC, the boundary condition is more complicated but similar. The functional is similarly given as

$$F(\mathbf{E}) = \int_\Gamma d\mathbf{r}\{(\nabla \times \mathbf{E}^*) \cdot [\mu^{-1}(\nabla \times \mathbf{E})] - k_0^2\varepsilon\mathbf{E}^*\mathbf{E}\}. \tag{9}$$

In the Secs. II B–II D, we first describe the formulation for the scaler Helmholtz equation, and then in Sec. II E we extend the formulation to the vector Helmholtz equation.

B. The GLL basis functions and discretization

To obtain discretized equations in the FEM framework for Eqs. (3) and (6), we use the GLL polynomials as the basis functions for the unknown fields E_z and H_z. The GLL polynomials can be used to interpolate a function with spectral accuracy, so that the error can be reduced exponentially by increasing the order of GLL polynomials. On the other hand, the GLL polynomials look similar to a local pulse function such as a Gaussian pulse with oscillations. These GLL basis functions can be used to expand piecewise smooth functions better than other lower-order basis functions such as linear basis functions used in the regular FEM. The Nth-order 1D GLL polynomials are defined as [16,17]

$$\phi_j^{(N)}(\xi) = \frac{-1}{N(N+1)L_N(\xi_j)}\frac{(1-\xi^2)L_N'(\xi)}{(\xi-\xi_j)}, \tag{10}$$

where $j=0,1,\ldots,N$, $L_N(\xi)$ is the Nth-order Legendre polynomial and $L_N'(\xi)$ is its derivative, ξ_j is the jth root of equa-

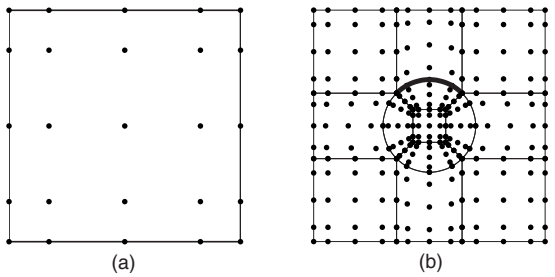

FIG. 1. (a) Locations of nodal points of the fourth-order SEM in the reference element. (b) SEM mesh and nodal points in the real space of one unit cell of square lattice 2D PC. There are four nodal points lying along the thick curve.

tion $(1-\xi^2)L_N'(\xi)=0$ which also gives the positions of nodal points in the SEM, and $\xi \in [-1,1]$. For our 2D problem, a basis function in the reference domain is written as the tensor product of two 1D basis functions, as given by

$$\tilde{\Phi}_{r,s}^{(N)}(\xi,\eta) = \phi_r^{(N)}(\xi)\phi_s^{(N)}(\eta), \tag{11}$$

where $\xi, \eta \in [-1,1]$. The distribution of nodal points (ξ_r, η_s) in the reference domain are shown in Fig. 1(a), with $N+1$ points in the ξ and η directions, respectively. After a curvilinear mapping between the real physical space (x,y) and reference space (ξ,η), a curved element in the physical space can be written in terms of the reference coordinates as $x=x(\xi,\eta)$, $y=y(\xi,\eta)$. Then the basis function in one curved physical element is $\Phi_{r,s}^{(N)}(x,y)=\tilde{\Phi}_{r,s}^{(N)}(\xi,\eta)$. From Fig. 1(a), we note that the distribution of nodal points is denser near the edge of an element than in the middle of the element. Since the field usually changes abruptly at the boundaries of different materials, this distribution of nodal points has great advantage of simulating systems with discontinuous dielectric materials.

In the SEM, the unit cell of a PC is divided into a number of nonoverlapping curvilinear quadrilateral elements conformal to the geometry, as illustrated in Fig. 1(b) for a square lattice. Each quadrilateral element is mapped into a reference square element in Fig. 1(a) with $(N+1)^2$ nodal points, where the nodal points on the element boundary are shared with the adjacent elements. Thus, the basis functions associated with nodal points interior to an element have the support in that element, while the basis functions associated with the nodal points on an element boundary have support on all the elements sharing that boundary. Furthermore, the basis functions associated with an outer boundary of the PC unit cell are shared by the element at the opposite side of the unit cell. As a result, if there are M independent basis functions (or nodal points) in a unit cell of the PC, the periodic part of the solution of the TM mode can be expanded by the basis functions within the unit cell as

$$U_E = \sum_{j=1}^{M} E_j \Phi_j^{(N)}(x,y), \tag{12}$$

where $j=\{r,s\}$ is a compound index of the basis functions. Equivalently, within each element, the field can be obtained by the basis functions as interpolation functions

$$U_E = \sum_{r,s=1}^{N} E_{r,s}\Phi_{r,s}^{(N)}(x,y), \tag{13}$$

where $E_{r,s}e^{i\mathbf{k}\cdot\mathbf{r}}$ is the electric field at the nodal point $[x(\xi_r,\eta_s), y(\xi_r,\eta_s)]$.

Inserting Eq. (12) in Eqs. (2) and (3) and applying the variational principle yields the eigenvalue equation

$$\mathbf{S}\cdot\mathbf{E} = k_0^2\mathbf{M}\cdot\mathbf{E}, \tag{14}$$

where $\mathbf{E}=[E_1,E_2,\ldots,E_M]^T$ is the unknown electric field vector, $\mathbf{S}$ and $\mathbf{M}$ are the stiffness matrix and mass matrix given by

$$\mathbf{S} = \sum_{e=1}^{N_e} \mathbf{S}^{(e)}, \quad \mathbf{M} = \sum_{e=1}^{N_e} \mathbf{M}^{(e)} \tag{15}$$

with elemental stiffness and mass matrices

$$S_{j,k}^{(e)} = \int_{\Gamma_e} d\mathbf{r}\{[(\nabla - i\mathbf{k}) \times \Phi_j^{(N)}\hat{z}]\mu_{rs}^{-1}[(\nabla + i\mathbf{k}) \times \Phi_k^{(N)}\hat{z}]\}, \tag{16}$$

$$M_{j,k}^{(e)} = \int_{\Gamma_e} d\mathbf{r}\Phi_j^{(N)}\varepsilon_{rz}\Phi_k^{(N)}, \tag{17}$$

where Γ_e is the area of the eth element and N_e is the total number of elements in the unit PC cell. The eigenvalue problem in Eq. (14) can then be solved to obtain the band structures. As discussed later, the SEM will have a simplified eigenvalue problem compared with the FEM.

C. Mapping of a curved element to the reference element

It is more convenient to calculate the integration in Eqs. (16) and (17) in the reference element than in the real space. The 2D mapping $x(\xi,\eta)$ and $y(\xi,\eta)$ can be expressed by functions of the four boundary curves of the element. Take $x(\xi,\eta)$ as an example: the functions of the four boundary curves of one element are $x(\xi,1)$, $x(\xi,-1)$, $x(1,\eta)$, and $x(-1,\eta)$. These could be straight lines or curves depending on the geometry, and can be given analytically or by interpolating some controlling points on the curved element. For example, a circular arc is given by $x=R\cos(\theta\eta)$, where R is the radius and θ the angular parameter. The two-dimensional mapping function is

$$\begin{aligned} x(\xi,\eta) = {} & \frac{1+\xi}{2}x(1,\eta) + \frac{1-\xi}{2}x(-1,\eta) \times \frac{1+\eta}{2}x(\xi,1) \\ & + \frac{1-\eta}{2}x(\xi,-1) - \left\{\frac{1+\eta}{2}\left[\frac{1+\xi}{2}x(1,1)\right.\right. \\ & \left. + \frac{1-\xi}{2}x(-1,1)\right] + \frac{1-\eta}{2}\left[\frac{1+\xi}{2}x(1,-1)\right. \\ & \left.\left. + \frac{1-\xi}{2}x(-1,-1)\right]\right\}. \end{aligned} \tag{18}$$

The mapping function for $y(\xi,\eta)$ is similar. The Jacobian matrix can be calculated as

$$\mathbf{J} = \begin{bmatrix} \frac{\partial x}{\partial \xi} & \frac{\partial y}{\partial \xi} & 0 \\ \frac{\partial x}{\partial \eta} & \frac{\partial y}{\partial \eta} & 0 \\ 0 & 0 & 1 \end{bmatrix}. \tag{19}$$

Making use of the formula [18]

$$\nabla \times \Phi_j^{(N)}(x,y)\hat{z} = \frac{1}{\det(\mathbf{J})}\mathbf{J}^T\tilde{\nabla} \times \tilde{\Phi}_{r,s}^{(N)}(\xi,\eta)\hat{z} \equiv \mathbf{f}_j \tag{20}$$

and $\Phi_j^{(N)}(x,y)\hat{z} = \tilde{\Phi}_{r,s}^{(N)}(\xi,\eta)\hat{z}$, $dxdy = \det(\mathbf{J})d\xi d\eta$, the integrations in Eqs. (16) and (17) are transferred to the reference coordinates as

$$S_{j,k}^{(e)} = \int_{-1}^{1}\int_{-1}^{1} d\xi d\eta \det(\mathbf{J})\{[\mathbf{f}_j - i\mathbf{k} \times \tilde{\Phi}_j^{(N)}\hat{z}] \times \mu_{rs}^{-1}[\mathbf{f}_k + i\mathbf{k} \times \tilde{\Phi}_k^{(N)}\hat{z}]\}, \tag{21}$$

$$M_{j,k}^{(e)} = \int_{-1}^{1}\int_{-1}^{1} d\xi d\eta \det(\mathbf{J})\tilde{\Phi}_j^{(N)}\varepsilon_{rz}\tilde{\Phi}_k^{(N)}. \tag{22}$$

The numerical integration is implemented by the GLL quadrature integration method. The Nth order GLL quadrature is exact for the integration of polynomials up to order $2N-1$. For an orthogonal element, the Jacobian is a constant matrix, and thus the integration with GLL quadrature of $N+1$ order gives the exact evaluation. For a curved element, the Jacobian is not polynomials in general, so we use higher order GLL quadrature, up to $N+6$, for the integration to obtain accuracy as high as 10^{-12}. However, as discussed below, we have also used the Nth-order GLL quadrature for this integration, which yields a diagonal mass matrix, thus a regular eigenvalue problem rather than a generalized eigenvalue problem. This further improves the efficiency of the SEM.

D. Diagonal mass matrix and regular eigenvalue problem

In addition to more accurate results and higher convergence rate, another advantage of the SEM over the FEM is that the generalized eigenvalue problem in Eq. (14) becomes a regular eigenvalue problem because of the orthogonality of the SEM basis functions. If we use GLL approximation [i.e., with only the Nth-order GLL quadrature to calculate the integration (22)], the quadrature points are exactly the same as the nodal points of GLL basis functions. As a result, the integration of the product of two Nth-order GLL basis functions is zero unless they are the same basis function. The consequence is that the mass matrix $M_{j,k}^{(e)}$ and hence $\mathbf{M}$ becomes diagonal. Thus, Eq. (14) can be converted into

$$\tilde{\mathbf{S}} \cdot \tilde{\mathbf{E}} = k_0^2\tilde{\mathbf{E}}, \tag{23}$$

where

$$\tilde{\mathbf{E}} = \mathbf{M}^{1/2} \cdot \mathbf{E}, \quad \tilde{\mathbf{S}} = \mathbf{M}^{-1/2} \cdot \mathbf{S} \cdot \mathbf{M}^{-1/2} \tag{24}$$

are trivial to obtain and the sparsity of matrix $\tilde{\mathbf{S}}$ is the same as $\mathbf{S}$. Note that the diagonal mass matrix applies even if the medium is in-plane anisotropic. Numerical results show that when the order of SEM basis functions is higher than 4, the difference between eigenvalue k_0 of Eqs. (14) and (23) converges as fast as the relative error of eigenvalues in Eq. (14). This means that the GLL quadrature approximation converges to the same result as the SEM with exact integration.

E. The mixed-order SEM for vector fields

In the case of full vector Helmholtz equation, the discretization of the equation and calculation of matrix elements are similar to those for a scaler Helmholtz equation. In order to suppress spurious, we employ the mixed-order SEM [17], which has a special choice of basis functions: The vector basis functions of the Nth order SEM in the reference domain have three kinds for three directions, which are given, respectively, as [17]

$$\tilde{\Phi}_{r,s}^{\xi}(\xi,\eta) = \phi_r^{(N-1)}(\xi)\phi_s^{(N)}(\eta),$$

$$\tilde{\Phi}_{r,s}^{\eta}(\xi,\eta) = \phi_r^{(N)}(\xi)\phi_s^{(N-1)}(\eta),$$

$$\tilde{\Phi}_{r,s}^{z}(\xi,\eta) = \phi_r^{(N)}(\xi)\phi_s^{(N)}(\eta). \tag{25}$$

The electric field in the reference domain is expanded as

$$\tilde{\mathbf{U}} = \sum_{u,r,s} \tilde{\Phi}_{r,s}^{u}(\xi,\eta), \tag{26}$$

where u takes the value $\hat{\xi}, \hat{\eta}, \hat{z}$, and then there are a total $(N+1)^2+2N(N+1)$ basis functions in one element corresponding to $(N+1)^2+2N(N+1)$ nodal points with each direction.

At the interface of two curvilinear quadrilateral elements, only the tangential field components need to be continuous. This means that not all of the nodal points on the element boundary are shared with the adjacent element. The covariant mapping which can keep the tangential components continuous is given as [18]

$$\mathbf{\Phi}_{r,s}^{u}(x,y) = \mathbf{J}^{-1}\tilde{\mathbf{\Phi}}_{r,s}^{u}(\xi,\eta),$$

$$\nabla \times \mathbf{\Phi}_{r,s}^{u}(x,y) = \frac{1}{\det(\mathbf{J})}\mathbf{J}^T\tilde{\nabla} \times \tilde{\mathbf{\Phi}}_{r,s}^{u}(\xi,\eta). \tag{27}$$

The superscript u on the left-hand side means the corresponding direction in real space. The direction can be spatially varying when the element is curved. Under this mapping, only the nodal points with direction tangential to the boundary of the element in the reference domain are shared with the adjacent element. The basis functions associated with the nodal points on an element boundary with tangential component to the boundary have support on all the elements sharing that boundary. In the two-dimensional problem, the size of element along $\hat{z}$ direction is infinitely large, so that the nodal points on a boundary with $\hat{z}$ direction is always tangential to the boundary. The basis functions associated with and tangential to an outer boundary of the PC unit cell are shared by the element at the opposite side of the unit cell

with a Bloch phase difference given in Eq. (8). As a result, if there are M independent basis functions in a unit cell of the PC, the electric field without the phase along $\hat{z}$ direction can be expanded by the basis functions as

$$\mathbf{U} = \sum_{j=1}^{M} E_j \mathbf{\Phi}_j(x,y), \tag{28}$$

where $j=\{u,r,s\}$ is a compound index of the basis functions.

Substituting Eq. (28) into Eq. (9), applying the variational principle and transferring the integration to reference coordinates result in an eigenvalue equation with the same form as Eq. (14), with the matrix elements given by

$$S_{j,k}^{(e)} = \int_{-1}^{1}\int_{-1}^{1} d\xi d\eta \det(\mathbf{J})\{[\mathbf{f}_j + ik_z\hat{z} \times (\mathbf{J}^{-1}\tilde{\mathbf{\Phi}}_j)]^* \times \mu^{-1} \cdot [\mathbf{f}_k + ik_z\hat{z} \times (\mathbf{J}^{-1}\tilde{\mathbf{\Phi}}_k)]\}, \tag{29}$$

$$M_{j,k}^{(e)} = \int_{-1}^{1}\int_{-1}^{1} d\xi d\eta \det(\mathbf{J})(\mathbf{J}^{-1}\tilde{\mathbf{\Phi}}_j)^* \varepsilon (\mathbf{J}^{-1}\tilde{\mathbf{\Phi}}_k), \tag{30}$$

where

$$\mathbf{f}_j \equiv \frac{1}{\det(\mathbf{J})}\mathbf{J}^T\tilde{\nabla} \times \tilde{\mathbf{\Phi}}_j(\xi,\eta). \tag{31}$$

III. NUMERICAL EXAMPLES

Numerical results of (a) a square lattice, (b) a triangular lattice isotropic dielectric rod PC, and (c) anisotropic square lattice, are shown in this section to validate the SEM for the band structures of PCs, and to test the accuracy of the method. The GLL quadrature integration approximation is used, which gives a diagonal mass and thus a regular eigenvalue problem. Furthermore, an anisotropic example is simulated to study the effects of anisotropy.

A. A PC with a square lattice

We have calculated the band structure of a square lattice 2D PC. It is composed of infinite length parallel alumina rods with relative permittivity $\varepsilon_r=8.9$ and radius $r=0.2a$ in the air, where a is the lattice constant. The SEM mesh with curved quadrilateral elements and all nodal points are shown in Fig. 1(b). In the unit cell, there are 13 curved quadrilateral elements, and 208 nodal points for the fourth order SEM. The band structure calculated with fourth order basis functions in the SEM is shown in Fig. 2 (marked by circles). For comparison, the band structure obtained by the PWE is also plotted in the figure (solid lines). The two sets of results agree well for both TE and TM modes.

To further understand the accuracy of the SEM, its numerical convergence behavior is examined by comparing the eigenvalue of the SEM results with various orders of basis functions with an accurate reference result obtained by a very high order SEM ($N=16$); note that we did not use the PWE results as the reference because the convergence of the PWE is not high enough (thus with lower accuracy). Our

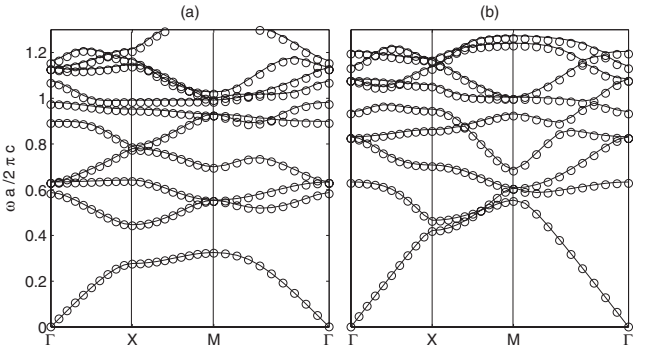

FIG. 2. Band structure of (a) TM mode and (b) TE mode of the 2D square-lattice PC formed by alumina rods with $\varepsilon_r=8.9$ and radius $r=0.2a$ in the air. Solid lines are results from the plane wave expansion method, and circles are results from the SEM.

numerical results from the SEM have shown that the relative error decreases to 10^{-12} as N increases to 14. Figure 3 shows the relative errors of the first and tenth band at X point of the first Brillouin zone of TM and TE modes versus (a) the number of SEM nodal points in the entire unit cell, and (b) the order of SEM basis functions. Figure 3(b) shows that the convergence curves are nearly straight lines in this semilog plot, indicating the spectral accuracy property for the SEM (i.e., the error decreases exponentially as N increases). The tenth-order solution converges slightly more slowly than the first-order solution because of its higher frequency. The relative errors for the second to ninth bands, which are not shown here for clarity, lie between those of the first and tenth bands. The errors of all bands decrease exponentially, suggesting that the SEM is an efficient tool for calculating the structures of higher bands because the errors of higher bands decrease nearly as fast as the first band.

The accuracy can be better characterized by the sampling density, or the number of nodal points per wavelength (PPW) in such wave applications. For an inhomogeneous problem, the value of sampling density depends on position as the wavelength in medium is spatially varying. Each element has a different number of nodal points per wavelength, thus the sampling density. The smallest sampling density dominates the error in the whole domain. As a result, we analyze the position with smallest sampling density, which is marked by

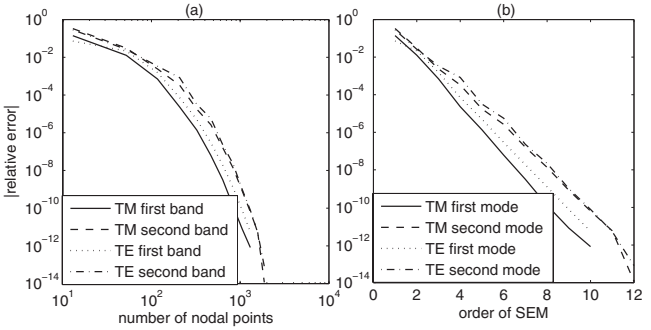

FIG. 3. (a) Relative error versus the number of nodal points for the eigenvalue at the X point of the first Brillouin zone of the first and the tenth bands in Fig. 2. (b) Relative error of the same data versus the order of SEM basis functions in a semilog scale plot.

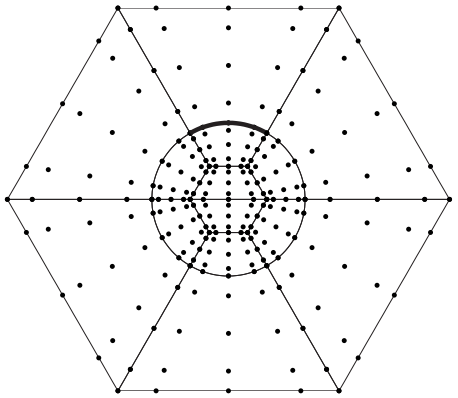

FIG. 4. The SEM mesh and nodal points in the real space of one unit cell of a triangular-lattice 2D PC. There are four nodal points lying along the thick curve.

a thick curve in Fig. 1(b). The length of the thick curve is $0.1\pi a$, and there are N nodal points along this line for the Nth order SEM basis functions. For a line with the same length outside the cylinder, there are also approximately N nodal points along the line, but the wavelength is three times larger in the cylinder than in the air because the relative permittivity of the cylinder is $\sqrt{8.9}$. For the tenth band, the frequency is about $1.2\omega a/2\pi c$, which corresponds to a wavelength in air region $a/1.2$ and wavelength in alumina rods $a/1.2\sqrt{8.9}$. This mean that along the thick curve, the sampling density is $N(a/1.2\sqrt{8.9})/(0.1\pi a) \approx 0.89N$ PPW. When we use $N=4$ (the fourth order SEM), the relative error is smaller than 10^{-3}, which is already acceptable in practical applications. This means that the SEM can give accurate results with a sampling density as small as 4 PPW.

The cost of SEM is much smaller than that of PWE. When we use the MIT photonic-bands package [6] to implement PWE, 256×256 resolution is needed to obtain the same accuracy as the fourth order SEM. This results in an eigenvalue problem of $65\,536\times65\,536$ matrix. In contrast, the fourth order SEM method results in 208 nodal points, which gives 208×208 stiffness and mass matrices. As to the CPU time, at the given resolution the PWE needs 36 s for each k point to calculate ten bands. The band structure with 30 k points needs 1080 s. For the implementation of SEM, we can first expand Eq. (21) into summation of three integration and extract the function of $\mathbf{k}$ out of the integration. After calculating all the integration in the expansion of Eqs. (21) and in Eq. (22), we can use the value of $\mathbf{k}$ for each k point to construct the stiffness matrix and obtain the mass matrix, respectively. In our implementation of fourth order SEM, the calculation of all the integration takes 42 s, and the construction of stiffness matrix and calculation of the ten lowest eigenvalues for each k point takes 0.5 s. Therefore, the band structure with 30 k points and ten bands needs 57 s, which is about 19 times smaller than the PWE.

B. A PC with a triangular lattice

Another example is a 2D PC with a triangular lattice. It is composed of dielectric cylinders with relative permittivity

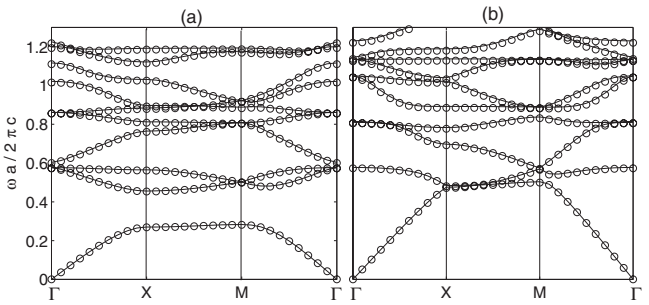

FIG. 5. Band structure of (a) TM mode and (b) TE mode of a 2D triangular-lattice PC formed by dielectric cylinders with $\varepsilon_r=11.4$ and radius $r=0.2a$ in the air. Solid lines are results from the plane wave expansion method, while circles are results from the SEM.

$\varepsilon_r=11.4$ and radius $r=0.2a$ in the air. The SEM mesh scheme as well as all the nodal points are shown in Fig. 4. There are 14 quadrilateral elements and 224 nodal points for the fourth order SEM. Similarly, the band structures for TE and TM modes with the fourth order basis functions in SEM are shown in Fig. 5 by circles, while the corresponding PWE results are plotted with solid lines for comparison. The relative errors of the first and the tenth bands at X point of the first Brillouin zone are plotted in Fig. 6 versus (a) the number of nodal points and (b) the order of SEM basis functions. It shows that the error decreases exponentially with N and as fast as that of the square-lattice 2D PC. The length of the thick curve in Fig. 4 is $0.2\pi a/3$ and the wavelength of the tenth band in the dielectric cylinder is about $a/1.2\sqrt{11.4}$, so that the sampling density along this curve is $N(a/1.2\sqrt{11.4})/(0.2\pi a/3) \approx 1.18N$. As a result, the fourth order SEM with five PPW is able to give acceptable accuracy with error smaller than 0.1%.

C. Effects of material anisotropy

Some materials such as gyromagnetic materials have anisotropic permittivity or permeability. The SEM is also suitable for the calculation of the band structures in such anisotropic media. Yttrium-iron-garnet (YIG) is one of this kind of material. When there is an external magnetic field along the z direction, the in-plane relative permeability is

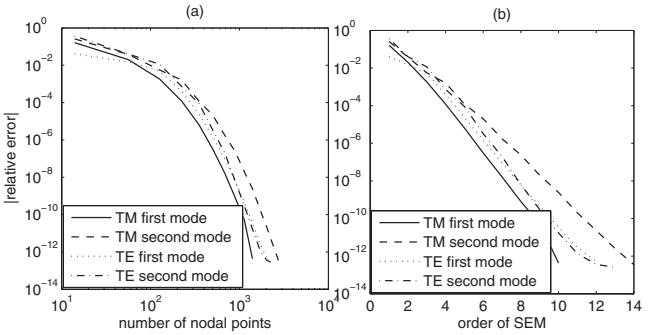

FIG. 6. (a) Relative error versus the number of nodal points for the eigenvalue at the X point of the first Brillouin zone of the first and the tenth bands in Fig. 5. (b) Relative error of the same data versus the order of SEM basis functions in a semilog scale plot.

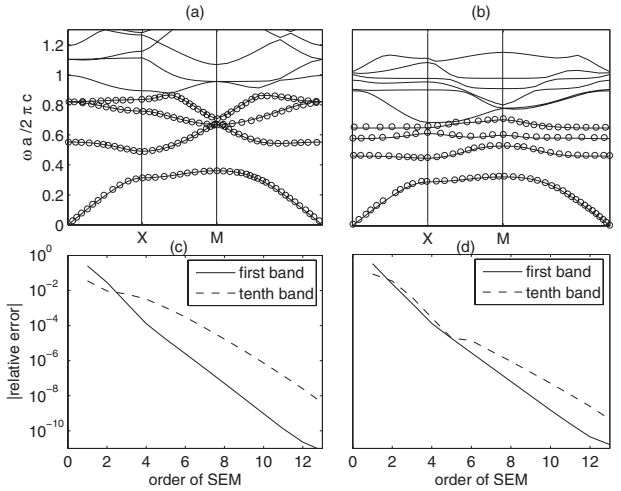

FIG. 7. TM mode band structure of square-lattice YIG cylinders with radius $r=0.11a$ with the applied magnetic field (a) $B_z=0$ ($\kappa=0$, $\mu=1$) and (b) $B_z=1600$ G ($\kappa=12.4$, $\mu=14$). As comparison, the results in Ref. [20] are plotted in circular points (only available for four bands). Relative error of the first and tenth band at X point (c) without and (d) with the applied magnetic field as a function of the SEM order.

$$\mu_{rs} = \begin{bmatrix} \mu & i\kappa \\ -i\kappa & \mu \end{bmatrix}. \tag{32}$$

If the applied magnetic field is zero, the off-diagonal value $\kappa=0$ and $\mu=1$. When the applied field is 1600 G, the tensor elements of YIG at 4.28 GHz are $\kappa=12.4$ and $\mu=14$. The relative permittivity of YIG is $\epsilon_{rz}=15$ [19]. We calculated the band structure of the photonic crystal design given in Ref. [20], which is a square lattice of YIG cylinders with radius $r=0.11a$. Figure 7 plots the band structure of TM mode (a) without and (b) with the applied magnetic field. Results for the first four bands from Ref. [20] are also plotted as circles for comparison. The convergence of the relative error of the first and tenth bands at X point versus the order of SEM basis functions is plotted in Fig. 7(c) and 7(d), respectively. We can observe the significant change of the band structure due to the applied magnetic field. Meanwhile, when the material is in-plane anisotropic, the convergence of relative error is as fast as that of an isotropic material.

D. Effects of out-of-plane propagation

When the out-of-plane propagation wave number k_z is nonzero, the TM and TE modes couple to each other as mentioned before. The full vector fourth-order SEM with mixed order basis functions is used to calculate the band structure with the out-of-plane propagation of the same 2D square lattice PC as that in Sec. III A. The 20 lowest bands that start at Γ point and X point are plotted in Figs. 8(a) and 8(b), respectively. When $k_z=0$, the stiffness and mass matrices reduce to two independent matrices for TM and TE modes, respectively. The submatrices for TM mode are exactly the same as that from the scaler SEM for TM mode; however, the submatrices for TE mode are totally different from the matrices produced by the scaler SEM for TE mode. Numerical results show that the relative error for TE mode of the vector SEM is also smaller than 0.1%. When k_z increases, the eigenvalues move upward as shown in Fig. 8. All of the bands move out of the light cone in free space when k_z is large, except for the first band starting from Γ point which starts out of the light cone at the beginning. Our experience of implementation of the vector SEM shows that there are no spurious modes with nonzero eigenvalues, and the number of spurious modes with zero eigenvalue is equal to the number of nodal points in the $\hat{z}$ direction.

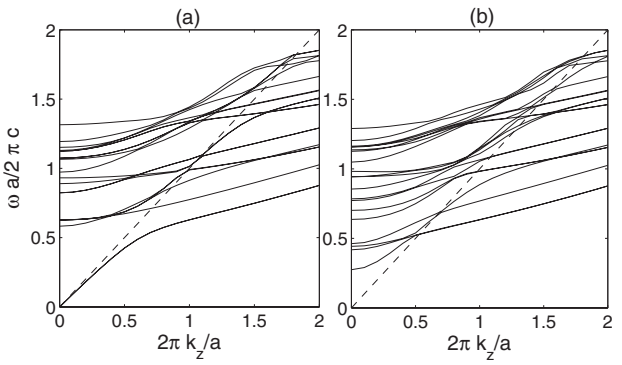

FIG. 8. Band structure of the out-of-plane propagation starting at (a) Γ point and (b) X point of the same 2D PC as in Fig. 2. The dash line in each figure is the light cone in free space.

IV. CONCLUSION

A higher-order finite element method, the spectral element method, is introduced to solve band structures of 2D anisotropic photonic crystals. Gauss-Lobatto-Legendre polynomials are used to construct the high-order basis functions in the spectral element method. Compared to the conventional finite element and finite difference methods, the SEM can have spectral accuracy with the error decreasing exponentially with the order of basis functions. Analytical mapping between the reference space and the real physical space with curved geometries allows accurate geometrical model in the SEM. Compared to the numerical results in Ref. [12], the relative error of SEM decrease faster than the multidomain pseudospectral method. The SEM has very good convergence of error for as high as the tenth band. A sampling density as small as four nodal points per wavelength can obtain acceptable accuracy. The method works well with in-plane anisotropic materials as well as with isotropic materials. When there is out-of-plane propagation, the full vector SEM gives results with the same accuracy. The method does not produce any spurious modes with nonzero eigenvalues, thus making it easy to distinguish the zero eigenvalue spurious modes from the real modes.

ACKNOWLEDGMENTS

The support from the National Science Foundation under Grant No. CCF-0621862 is appreciated. The support from the NBRPC under Grant No. 2007CB935500, from the NSFC under Grants No. 10574163 and No. 90306016, and from the CSC under Grant No. 2007102844 is appreciated.

[1] E. Yablonovitch, Phys. Rev. Lett. **58**, 2059 (1987).
[2] S. John, Phys. Rev. Lett. **58**, 2486 (1987).
[3] J. D. Joannopoulos, *Photonic Crystals: Molding the Flow of Light*, 2nd ed. (Princeton University Press, Princeton, 2008).
[4] Yoshihiro Akahane, Takashi Asano, Bong-Shik Song, and Susumu Noda, Nature (London) **425**, 944 (2003).
[5] C. P. Yu and H. C. Chang, Opt. Express **12**, 1397 (2004).
[6] S. G. Johnson and J. D. Joannopoulos, Opt. Express **8**, 173 (2001).
[7] K. M. Ho, C. T. Chan, and C. M. Soukoulis, Phys. Rev. Lett. **65**, 3152 (1990).
[8] Q. H. Liu, Microwave Opt. Technol. Lett. **15**, 158 (1997).
[9] B. Yang, D. Gottlieb, and J. S. Hesthaven, J. Comput. Phys. **134**, 216 (1997).
[10] G.-X. Fan, Q. H. Liu, and J. S. Hesthaven, IEEE Trans. Geosci. Remote Sens. **GE–40**, 1366 (2002).
[11] Q. H. Liu, IEEE Antennas Wireless Propag. Lett. **1**, 131 (2002).
[12] P.-J. Chiang, C.-P Yu, and H.-C. Chang, Phys. Rev. E **75**, 026703 (2007).
[13] B. G. Ward, IEEE J. Quantum Electron. **44**, 150 (2008).
[14] P. Sotirelis and J. D. Albrecht, Phys. Rev. B **76**, 075123 (2007).
[15] J.-H. Lee and Q. H. Liu, IEEE Trans. Comput.-Aided Des. **24**, 1848 (2005).
[16] Gary C. Cohen, *Higher-Order Numerical Methods for Transient Wave Equations* (Springer, Berlin, 2001).
[17] J.-H. Lee, T. Xiao, and Q. H. Liu, IEEE Trans. Microwave Theory Tech. **54**, 437 (2006).
[18] A. F. Peterson, S. L. Ray, and R. Mittra, *Computational Methods for Electromagnetics* (IEEE Press, Piscataway, NJ, 1997).
[19] D. M. Pozar, *Microwave Engineering* (Wiley, New York, 1998).
[20] Z. Wang, Y. D. Chong, J. D. Joannopoulos, and M. Soljacic, Phys. Rev. Lett. **100**, 013905 (2008).